# $x$-hour Outdoor Photometric Stereo

Yannick Hold-Geoffroy[1], Jinsong Zhang*[2], Paulo F. U. Gotardo[3], and Jean-François Lalonde†[1]

[1]Laval University, Quebec City
[2]Beihang University, Beijing
[3]Disney Research, Pittsburgh

## Abstract

*While Photometric Stereo (PS) has long been confined to the lab, there has been a recent interest in applying this technique to reconstruct outdoor objects and scenes. Unfortunately, the most successful outdoor PS techniques typically require gathering either months of data, or waiting for a particular time of the year. In this paper, we analyze the illumination requirements for single-day outdoor PS to yield stable normal reconstructions, and determine that these requirements are often available in much less than a full day. In particular, we show that the right set of conditions for stable PS solutions may be observed in the sky within short time intervals of just above one hour. This work provides, for the first time, a detailed analysis of the factors affecting the performance of $x$-hour outdoor photometric stereo.*

## 1. Introduction

Since its inception in the early 80s, Photometric Stereo (PS) [23] has been explored under many an angle. Whether it has been to improve its ability to deal with complex materials [4] or lighting conditions [6], the myriad of papers published on the topic are testament to the interest this technique has garnered in the community. While most of the papers on this topic have focused on images captured in the lab, recent progress has allowed the application of PS on images captured outdoors, lit by the more challenging case of uncontrollable, natural illumination.

A central question to any PS practitioner is that of the quality and amount of data required to achieve good performance. What should the lighting conditions be during data capture? How many images (illumination conditions) are needed? What is the shortest time interval required to collect these samples?

In the lab, theoretical analyses for Lambertian surfaces, lit by point light sources, reveal that the minimum number of images is three [23] and that the optimal light configuration yields an orthogonal triplet of light directions [9]. While such theoretical guarantees are reassuring, they are however much harder to obtain for the case of more complex, non-Lambertian reflectance, or with more general lighting models. Thus, practitioners are left without guidance in the task of determining when to stop capturing data, an inherently tedious trial-and-error process. As a result, it is not rare for PS datasets to include hundreds of images [4] in an uncertain attempt to obtain accurate reconstruction.

While capturing more data in the lab can be done relatively easily, the same cannot be said for outdoor imagery. Indeed, one does not control the sun and the other atmospheric elements in the sky; so one must wait for lighting conditions to change on their own. A creative solution to this problem was proposed in [15], but it is limited to objects that can be placed on a small moving platform. Therefore, capturing more data for fixed, large objects still means waiting days, or even months, potentially [1, 2].

Luckily, techniques that reduce the requirement to a single day's worth of data have also been proposed [18, 20, 24]. However, this is still much longer than what can be done in the lab, where light sources can be waved around rapidly and data be captured in minutes. And although recent work has investigated which days provide more favorable atmospheric conditions for outdoor PS [13, 20], so far, no study has systematically demonstrated the performance of outdoor PS with less than a full day's worth of data. Is a full day of observations indeed necessary to obtain good results in outdoor PS? Or could similar results be obtained over a shorter time interval (say, 1 hour)? If so, what should be happening in the sky over that time interval? Besides easing the requirements on data capture, these questions are also important in that, in future work, they could extend the applicability of outdoor PS to new scenarios (*e.g.*, to more quickly capture non-static outdoor objects that show grad-

*Research done while Jinsong Zhang was an intern at Laval University.
†Contact author: jflalonde@gel.ulaval.ca

ual changes in shape or appearance over time).

This paper presents what are believed to be the first answers to the questions above. Here, we seek to determine the relationship between expected PS performance (in normal estimation) and: 1) the duration of data capture within a single, arbitrary day; and 2) specific atmospheric events that introduce beneficial lighting variations during that time interval. To achieve this goal, we use a large database of natural, outdoor illumination (sky probes) [13], take a detailed look at the conditions under which normals can be reconstructed reliably, and explore whether these conditions occur over less than one day.

**Dataset** Our analysis is based on the dataset of [13, 14], which provides wide angle, high dynamic range (HDR) images of the sky hemisphere. It contains more than 3,800 different illumination conditions captured over 23 different days. Each HDR sky photograph span the full 22 stops required to properly capture outdoor lighting using the approach proposed in [22]. The photos are also temporally aligned, and were captured every day from 10:30 until 16:30 (see supplementary material). Since this database captures only the sky hemisphere, we synthesized an infinite Lambertian ground plane with an albedo equal to that of asphalt ($\rho \approx 0.15$ [3]). Finally, the images were converted to grayscale before the analysis was performed.

## 2. Related work

A complete review of PS approaches is beyond the scope of this paper. For conciseness, we focus on more closely related work that have considered PS on outdoor conditions.

The first works attempting PS reconstruction on outdoor data [1, 2] made the observation that, over the course of a day, the sun seems to move on a planar path through the sky. Unfortunately, co-planar light sources yield an under-constrained, two-source PS problem [12], which cannot be solved without strong regularization and reconstruction artifacts. To avoid this issue, the authors therefore propose gathering months of data using webcams.

Recently, Shen *et al.* [20] showed that, contrary to common belief, the sun path in the sky actually does not always lie within a plane. Thus, PS reconstruction can sometimes be computed in a single day even with a point light source model. The main downside of this approach is that planarity of the sun path (*i.e.*, conditioning of PS reconstruction) depends on the latitude and the time of year. More specifically, reconstruction becomes unstable at high latitudes near the winter solstice, and worldwide near the equinoxes.

To compensate for limited sun motion, other approaches have proposed using richer models of illumination that account for additional atmospheric factors in the sky. Typically, this is done by employing (hemi-)spherical environment maps [7]. On one hand, full environment maps can be captured and used with calibrated PS algorithms [15,21,24]. On the other hand, it is also possible to estimate part of the environment map without explicitly capturing it, by synthesizing a hemispherical model of the sky using physically-based models [16, 18]. While these richer models do allow reconstructions from only one day, it is unknown whether the same could be done with even less data.

The work presented below extends our initial analysis in [13]. Rather than presenting a new reconstruction algorithm, in [13] we conducted an empirical analysis of the same sky database to identify which days provide more favorable atmospheric conditions for outdoor PS. However, no consideration was given to the shortest time interval of data capture needed to obtain accurate reconstructions; all results were reported on at least 6 hours (a "full day") of captured data. Here, instead of comparing days, we focus on analyzing different time intervals within each day. We then show that 6 hours is actually more than necessary, and detail the relationship between the appearance of the sky hemisphere and the quality of PS reconstruction.

Finally, it is also worth mentioning shape-from-shading techniques such as [5, 17, 19], which push reconstruction to its limits by attempting to recover shape from a single input image. In this case, the information provided by the shading cue is obviously insufficient to define a unique solution, so these approaches rely strongly on priors of different types and complexities. In this paper, we avoid such strong priors and focus our analysis exclusively on the photometric/shading cues obtained from multiple images.

## 3. Outdoor PS conditioning

In the following, we consider a small planar surface patch with normal vector $\mathbf{n}$ and Lambertian reflectance with albedo $\rho$. As discussed in [13, 15], the lighting contribution of an environment map to a Lambertian surface patch can be formulated as in an equivalent problem with a single point light source $\bar{\mathbf{l}} \in \mathbb{R}^3$. This vector is the mean of the light vectors computed over the hemisphere of incoming light directions defined by $\mathbf{n}$. This virtual point light source $\bar{\mathbf{l}}$ is henceforth referred to as the *mean light vector* (MLV). It is important to note that, as opposed to the traditional PS scenario where point light sources are fixed and thus independent of $\mathbf{n}$, here the *per-pixel* MLV is a function of $\mathbf{n}$. Thus, patches with different orientations define different sets of MLVs (as discussed later and shown in fig. 3).

Given multiple images of the same patch, taken at different times, we collect all photometric constraints for that patch and obtain the PS equation in matrix form:

$$\mathbf{b} = \begin{bmatrix} b_1 \\ b_2 \\ \vdots \\ b_T \end{bmatrix} = \begin{bmatrix} \bar{\mathbf{l}}_1^T \\ \bar{\mathbf{l}}_2^T \\ \vdots \\ \bar{\mathbf{l}}_T^T \end{bmatrix} \mathbf{x} = \mathbf{L}\mathbf{x}\,, \tag{1}$$

where $b_i \in \mathbb{R}$ are the observed pixel intensities, and $\mathbf{x} \in \mathbb{R}^3$ is the surface normal $\mathbf{n}$ scaled by $\rho$.

Let $\hat{\mathbf{x}} = (\mathbf{L}^T\mathbf{L})^{-1}\mathbf{L}^T\mathbf{b}$ denote the least-squares solution of (1). A 95% confidence interval for normal $\mathbf{x}$ is given by

$$\hat{\mathbf{x}} \pm \boldsymbol{\delta}\,, \quad \text{with } \delta_k = 1.96\frac{\sigma}{\rho}\lambda_k\,, \tag{2}$$

where $\sigma$ is the camera noise level and $\lambda_k$ is the square root of the $k$-th element on the diagonal of $(\mathbf{L}^T\mathbf{L})^{-1}$ [11].

From (2), note that the only light-dependent stability factor in the confidence interval $\boldsymbol{\delta}$ is $\lambda_k$; the other two factors are related to the camera ($\sigma$), and surface reflectance ($\rho$). In this paper, we analyze the maximum uncertainty $\lambda_{\max} = \max_k(\lambda_k)$, as a conservative performance measure that is independent of albedo and sensor noise; $\lambda_{\max}$ is a *maximum noise gain* factor, *i.e.*, the intensity of noise amplification in the solution. Here, we are interested in (*i*) investigating how the noise gain $\lambda_{\max}$ is influenced by the duration of outdoor data capture, and in (*ii*) identifying specific changes, or *events*, in outdoor lighting that are associated with more stable PS solutions (smaller $\lambda_{\max}$).

To make our analysis tractable, we do not model cast shadows and inter-reflections. In addition, we assume that the sky hemisphere (around zenith) provides the dominant part of incoming light. Unless stated otherwise, our simulations consider a day near an equinox, which corresponds to the worst case scenario with coplanar sun directions [20].

## 4. $x$-hour outdoor PS

This section provides the first answers to the questions raised above by looking at collections of mean light vectors (MLVs) from both simulated and real sky data. The main goal is to analyze the behavior of the illumination factors $\lambda_k$ (and associated confidence interval) of normal estimation. More specifically, we investigate numerical stability (MLV coplanarity) as a function of the apparent sun motion and cloud coverage within capture intervals of different durations, containing different atmospheric events. We also compare the resulting performance measures of $x$-hour outdoor PS to those of full-day outdoor PS.

### 4.1. Cloud coverage and MLV shifting

As shown in [13], with data captured under clear skies, the MLVs of the model above will point nearly towards the sun, from which arrives most of the incoming light. Thus, near an equinox (worldwide), the resulting set of MLVs are nearly coplanar [20], resulting in poor performance, fig. 1(a). For a day with an overcast sky, performance is also poor because the set of MLVs are nearly colinear and shifted towards the patch normal $\mathbf{n}$, fig. 1(b). Finally, in partly cloudy days (mixed skies), the sun is often obscured by clouds and such occlusion shifts some MLVs away from the solar plane, improving numerical stability, fig. 1(c).

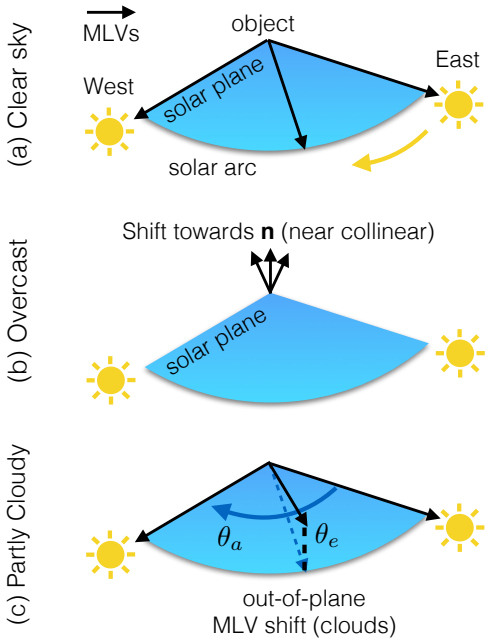


Figure 1. Impact of cloud coverage on the numerical conditioning of outdoor PS: clear (a) and overcast (b) days present MLVs with stronger coplanarity; in partly cloudy days (c) the sun is often obscured by clouds, which may lead to out-of-plane shifts of MLVs.

### 4.2. Solar arcs and MLV elevation

Here, we seek to provide a sense of the minimal length of solar arc and amount of out-of-plane MLV shift required in single-day outdoor PS.

Assuming a day near an equinox, the apparent sun trajectory worldwide describes an arc $\theta_a$ within the solar plane of about $15^\circ$ per hour. We now use this observation to evaluate the numerical stability of outdoor PS for data capture intervals (solar arcs) of different lengths. Considering a partly cloudy sky, we also investigate the interaction of solar arc and cloud coverage; we quantify performance as a function of both acquisition time (solar arc $\theta_a$) and amount of out-of-plane MLV shift (elevation angle $\theta_e$) introduced by clouds.

A simple and effective way to investigate conditioning with different capture scenarios is to consider a simulation with the minimum number of three MLVs, as required for outdoor PS using (1). We simulate solar arcs $\theta_a$ of different lengths by defining two MLVs on a reference solar plane, with the third MLV presenting varying elevation $\theta_e$ away from this plane, as illustrated in fig. 1(c). The actual orientation of the solar plane varies with the latitude of the observer; thus, we represent MLV shift relative to this plane.

The numerical conditioning of outdoor PS, as observed with different configurations for these three MLVs, is then scored using the noise gain $\lambda_{\max}$ (sec. 3). This measure is independent of albedo and sensor noise; it is also related to the condition number of the illumination matrix $\mathbf{L}$ in (1).

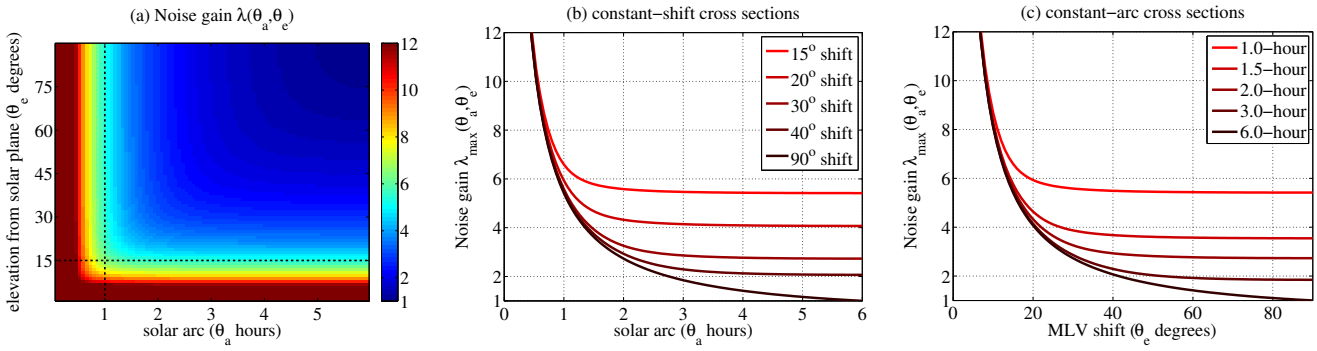


Figure 2. Simulated noise gain $\lambda_{\max}(\theta_a, \theta_e)$ as a function of solar arc $\theta_a$ and MLV shift (elevation) angle $\theta_e$. See discussion in the text.

We compute $\lambda_{\max}(\theta_a, \theta_e)$ for solar arcs $\theta_a$ of up to 6 hours ($90°$) and MLV elevations $\theta_e$ up to $90°$. For simplicity, we consider triplets of unit-length MLVs—thus, conditioning depends on the magnitude $\sin(\theta_e)$ of the out-of-plane component of the third MLV. Clearly, the optimal noise gain $\lambda_{\max} = 1$ is obtained when the MLVs are mutually orthogonal ($\theta_a = \theta_e = 90°$).

Fig. 2(a) shows that the noise gain $\lambda_{\max}$ drops quickly to under 6 for capture intervals at just above 1 hour and for MLV shifts $\theta_e > 15^0$. This result suggests that even the performance of 1-hour PS can be acceptable with small levels of sensor noise $\sigma$ and high surface reflectance $\rho$. To ease visualization, figs. 2(b,c) show cross sections of the $\lambda_{\max}(\theta_a, \theta_e)$ gain surface for a constant shift or solar arc.

A second important prediction from fig. 2, considering (more realistic) small to moderate amounts of MLV shifts $\theta_e \leq 40°$, is that conditioning will improve very little for data capture intervals above 3 hours ($45°$ solar arcs). Reducing data capture from 3 to 2 hours would lead to an additional increase in uncertainty ($\lambda_{\max}$) of less than $30\%$ (from about 2.8 to nearly 3.6). Still, 2-hour outdoor PS with noise gains under $4\times$ may be possible if an MLV shift of $\theta_e > 20°$ is introduced by atmospheric events during capture. Uncertainty in the results of 1-hour outdoor PS would be about 5 to 7 times that of full-day (6-hour) outdoor PS.

### 4.3. MLV shifts in real sky probes

While the analysis above suggests that outdoor PS may be possible with a capture interval of only about 1 to 3 hours, it does not answer whether it is possible to observe an adequate amount of MLV shift (elevation away from solar plane) within a single partly cloudy day. In the following, we analyze the shifting (coplanarity) of real MLVs obtained from a database of real environment maps (sky probes) [13].

First, it is important to note that surface patches of different orientations (normals) are exposed to different hemispheres of illumination, with light arriving from above (sky) and below (ground). This fact is illustrated in fig. 3 for three different normal vectors (rows) and two different days (columns). Each globe represents the coordinate system for the environment maps captured in a day. For each combination normal-day, the time-trajectory of computed MLV directions (dots) and intensities (colors) are shown on the globe. Brighter MLVs lie closely to the solar arc, while darker MLVs may shift away from it.

To more closely match the scenario considered above, we scale these real MLVs so that the brightest one over all days (*i.e.*, for the most clear sky) has unit-length. From fig. 3, also note that some MLVs are shifted very far from the solar arc but, as indicated by the darker colors, their intensity is dimmed considerably by cloud coverage; little improvement in conditioning is obtained from these MLVs.

Most important, fig. 3 shows that the amount of out-of-plane MLV shift (elevation) relative to the solar arc also depends on the orientation $\mathbf{n}$ of the surface patch. This suggest that outdoor PS reconstruction may present different amounts of uncertainty (conditioning) depending on the normal of each patch. Indeed, the noise gain ($\lambda_{\max}$) values in fig. 4 show that patches with nearly horizontal normals (orthogonal to the zenith direction) are associated with sets of MLVs that are closer to being coplanar throughout the day. As expected, patches oriented towards the bottom also present worse conditioning since they receive less light.

Although these MLVs were computed from environment maps captured in the Northern hemisphere (Pittsburgh, USA, and Quebec City, Canada [13]), similar conclusions can be drawn for the Southern hemisphere. Finally, note that this section has considered MLV shifts in whole-day datasets. Next, we look at subsets of MLVs from time intervals of varying lengths and analyze some of the atmospheric events associated with improved conditioning.

### 4.4. Evolution of noise gain over time

In this section, we show how the conditioning of outdoor PS evolves over time. Analyzing the patterns in its evolution will allow us to isolate important "events"—points at which uncertainty suddenly drops—and investigate whether such events occur in close succession.

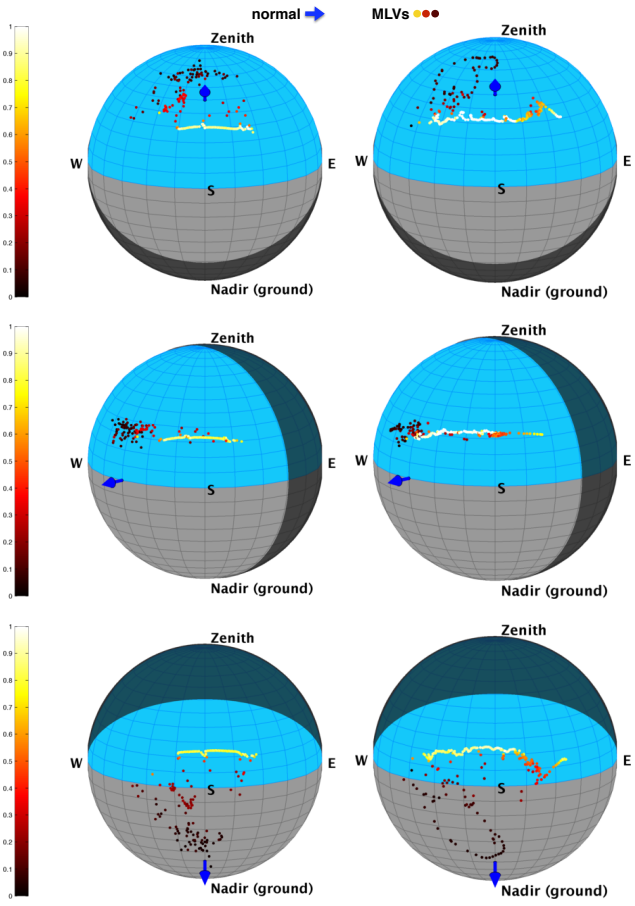


(a) Mixed clouds (06-NOV-13) (b) Mixed clouds (11-OCT-14)

Figure 3. Globes representing the coordinate system of sky probes. Each normal (blue arrow) defines a shaded hemisphere in the environmental map that does not contribute light to the computed MLVs (dots). All MLVs in two particular partly cloudy days (columns) were computed from real environment maps [13] for 3 example normal vectors (rows). Relative MLV intensities are shown in the color bar on the left. See also video in [14].

The main results are given in fig. 5, which plots the gain factor $\lambda_{\max}$ for all possible time intervals in four different days. Since $\lambda_{\max}$ varies with $\mathbf{n}$, we plot the median gain over 321 normal vectors visible to the camera (by subdividing an icosahedron three times) for each time interval.

The first row of fig. 5(a,b) illustrates the case of two days identified in sec. 4.1 as yielding poor outdoor PS reconstructions. As seen in the plots, low noise gains are never reached, irrespective of the start time and duration of the capture interval. We note that the (nearly) overcast sky of fig. 5(b) exhibits better behavior than the completely clear sky of fig. 5(a). This is because that day is not completely overcast, and the sun sometimes becomes visible (see the sun log-intensity plot). MLVs are thus shifted away from their main axes, while improving conditioning only slightly.

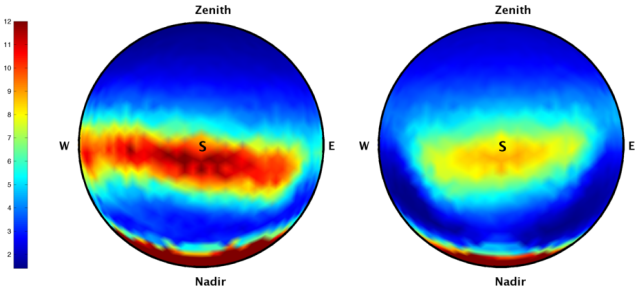


(a) 06-NOV-13 (b) 11-OCT-14

Figure 4. Noise gain for each normal direction $\mathbf{n}$ visible to the camera; the colors indicate the shifting (coplanarity) of the associated MLVs. The camera is assumed to lie to the South of this hypothetical target object. For both days, normals that are nearly horizontal are associated with more coplanar MLVs (smaller shifts, higher gains). These normals define a *zero-crossing region* between positive and negative out-of-plane shifts (mid row in fig. 3), where occlusion of the sun results in shifts that are predominantly *along* the solar arc. See also video available in [14].

More interesting scenarios arise on days exhibiting a better mix of sun and moving clouds, such as the two examples in fig. 5(c,d). The two black vertical lines in fig. 5(c) identify capture intervals starting at two different times. Following the line labeled "start time 1" (beginning at 11:00), we notice that uncertainty remains high for approximately two hours, then suddenly drops at around 13:00. This time instant is followed by sudden changes in sun intensity (due to passing clouds) that are sufficient to shift the MLV away from the sun plane. Subsequently, uncertainty continues to decrease, albeit at a much slower pace, over the rest of the day. The second time interval (identified as "start time 2") starts at 14:00, so it does not benefit from that period of sun intensity changes. The maximum gain at the end of the interval is therefore higher.

Of course, this could be due to a simple fact: the first interval is longer than the second one. However, fig. 5(d) shows that longer intervals do not always result in lower uncertainty. This time, two 2-hour intervals are considered. The time interval labeled as "start time 1" stops right before the 14:00 mark, and only sees clear skies; as expected, the uncertainty is very high. "Start time 2", beginning at 13:30, can fully exploit the MLV shifts caused by moving clouds to dramatically decrease PS uncertainty, even while the interval length is kept constant.

### 4.5. Overall performance of $x$-hour PS

We noted in fig. 5(d) that sufficient conditions for low uncertainty could be met in as little as 2 hours. In this section, we evaluate how often one can achieve low uncertainty in short time intervals. This is done by assessing the distribution of noise gains from short time intervals, and aggregating results over multiple days.

To compute these statistics, we first consider a single

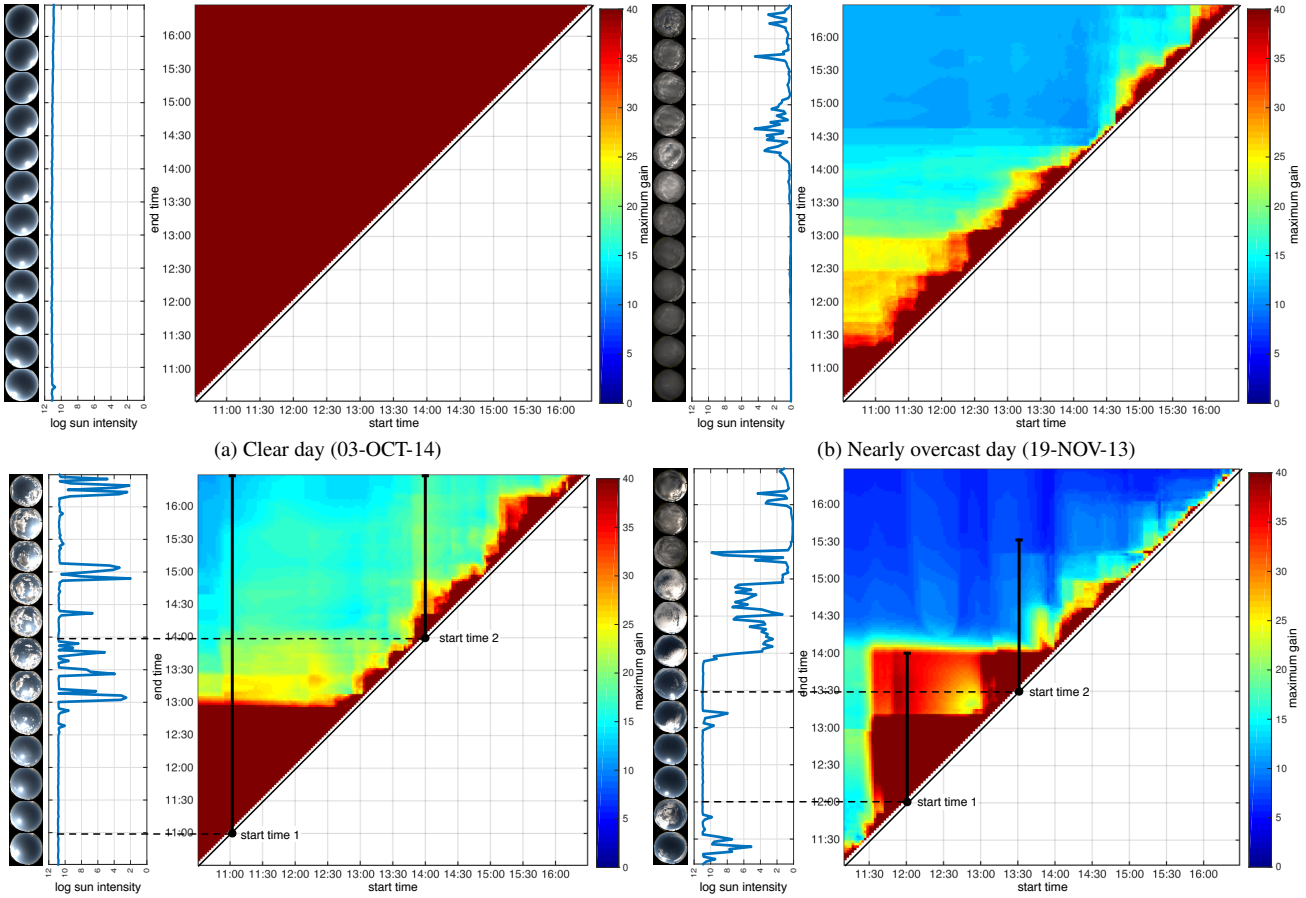


(a) Clear day (03-OCT-14)

(b) Nearly overcast day (19-NOV-13)

(c) Clear sky and mixed clouds (24-AUG-13)

(d) Mixed clouds (06-NOV-13)

Figure 5. Fine-grained analysis of the expected uncertainty of outdoor PS as a function of time over four selected days in the dataset. Colored plots show the maximum gain $\lambda_{\max}$ as a function of start time (diagonal along the plot), and duration of the interval. The black lines identify particular time intervals discussed in the text. The blue curve to the left of each colored plot represents the log sun intensity over the course of that day. Photographs of the sky for each day are also shown on the left.

normal and a single day. For a particular time interval $\tau = \{t_{\text{start}}, t_{\text{end}}\}$, we compute the ratio $r_\lambda(\tau)$ of its noise gain divided by the best (minimum) gain of all possible intervals in this day (including the full-day interval). Fig. 6(a,b) shows distributions of relative gains $r_\lambda$ for the two days in fig. 5(c,d). Fig. 6(a) shows that, for intervals of 4 hours, 75% of the normals have uncertainty below twice the minimum gain for that day. In the case of fig. 6(b), that interval drops to 3 hours.

The ratios $r_\lambda$ were then computed for all normals, over all days in the database. The compound statistics are shown in fig. 6(c). They empirically illustrate that there were many opportunities for stable normal reconstruction with short capture intervals. For example, more than 50% of the time intervals of 3 hours resulted in reconstructions that had at most twice the uncertainty of the optimal interval. These results suggest that opportunities for shorter capture sessions seem to occur quite frequently in practice.

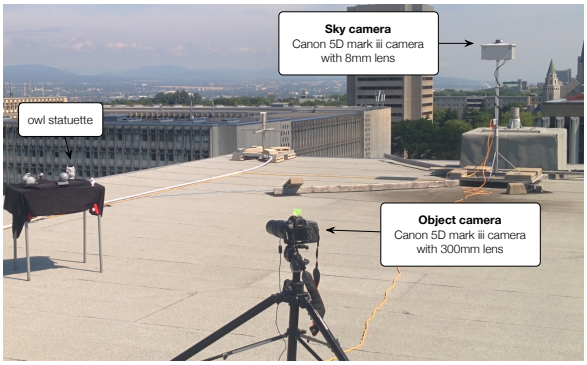


Figure 8. Real data capture setup. HDR photographs of the sky and of the object (owl statuette) are simultaneously captured by two cameras installed on the roof of a tall building.

## 5. Experimental validation

We validate the analyses in sec. 3 and 4 via calibrated outdoor PS on synthetic and real object images with known

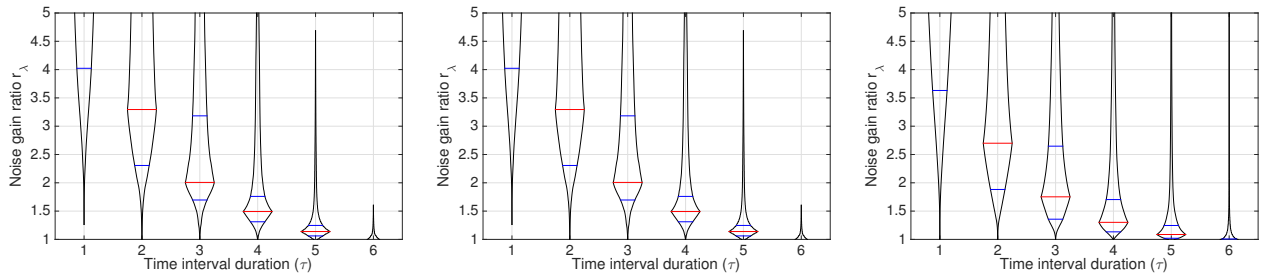


(a) 24-AUG-13 (b) 06-NOV-13 (c) Entire dataset

Figure 6. Distribution of noise gain ratio $r_\lambda(\tau)$ as a function of time interval duration: (a,b) two days in fig. 5; (c) across all the dataset. The distributions of computed ratios are displayed vertically as "box-percentile plots" [10]; the red horizontal bars indicate the median, while the bottom (top) blue bars are the 25th (75th) percentiles.

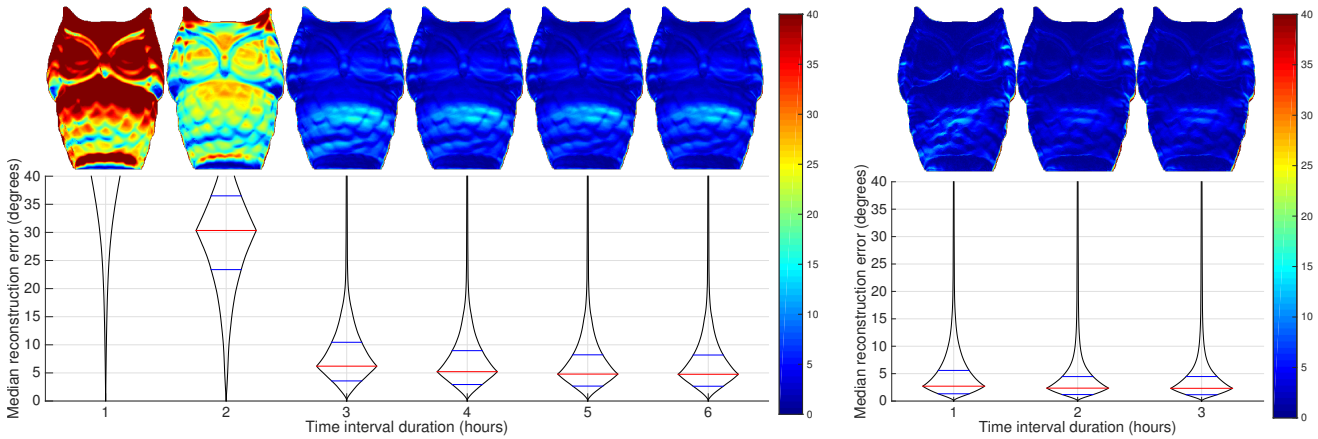


(a) Intervals starting at 12:00 on 06-NOV-13 (b) Intervals starting at 13:30 on 06-NOV-13

Figure 7. Normal recovery error as a function of time interval and start time: (a) 12h00 and (b) 13h30 on 06-NOV-13. Experiments are performed on a synthetic object rendered with real sky probes and additive Gaussian noise $\sigma = 1\%$. The top row shows per-pixel angular error, color-coded as in the scale on the right. The bottom row shows box-percentile error plots (see fig. 6). As suggested in fig. 5(d), the performances of $\{3,4,5,6\}$-hour outdoor PS are very similar (a). Even 1-hour outdoor PS can be competitive if started at the right time (b).

ground truth normals. These normals are used as an optimal initialization for computing ground-truth MLVs, thus avoiding convergence issues of nonlinear optimization and allowing us to focus on assessing errors due to illumination effects in the real sky probes. We then perform calibrated outdoor PS on these images using the algorithm in [24], with the following two differences: (*i*) we use all possible pairs of images to compute ratios, instead of selecting a single denominator image; and (*ii*) we apply anisotropic regularization [12] to mitigate the impact of badly-conditioned pixels on the surface reconstruction.

**Synthetic data** We first consider synthetic images of an owl model rendered with real sky probes. The rendered images were perturbed with additive Gaussian noise at 1% the median pixel intensity. For each image, one real-world environment map from the database was used as the sole light source. Cast shadows were not simulated to isolate the analysis to the photometric cue alone (see [14] for more realistic results with a physically-based rendering engine).

We ran calibrated outdoor PS on all time intervals starting at 12:00 or 13:30 for the day 06-NOV-13 (see fig. 5(d)), in increments of one hour. The main results of this experiment are shown in fig. 7. Fig. 7(a) follows "start time 1" in fig. 5(d); the reconstruction error improves significantly until an interval of 3 hours is reached, at which point the error improves only slightly through the rest of the day. Thus, the additional data provides little new information. In fig. 7(b), we now follow the path of "start time 2" in fig. 5(d); in this case, the error is already quite low after just one hour.

**Real data** Another similar experiment considered real photos of a real owl statuette. To capture this data, we set up two cameras on the roof of a tall building as shown in fig. 8. The first camera, dubbed "sky camera", captures omnidirectional photos of the sky using the approach proposed by Stumpfel *et al.* [22]. The second, "object" camera is equipped with a telephoto zoom lens and captures photos of the statuette. Both cameras capture exposure-bracketed HDR photos simultaneously, once every two min-

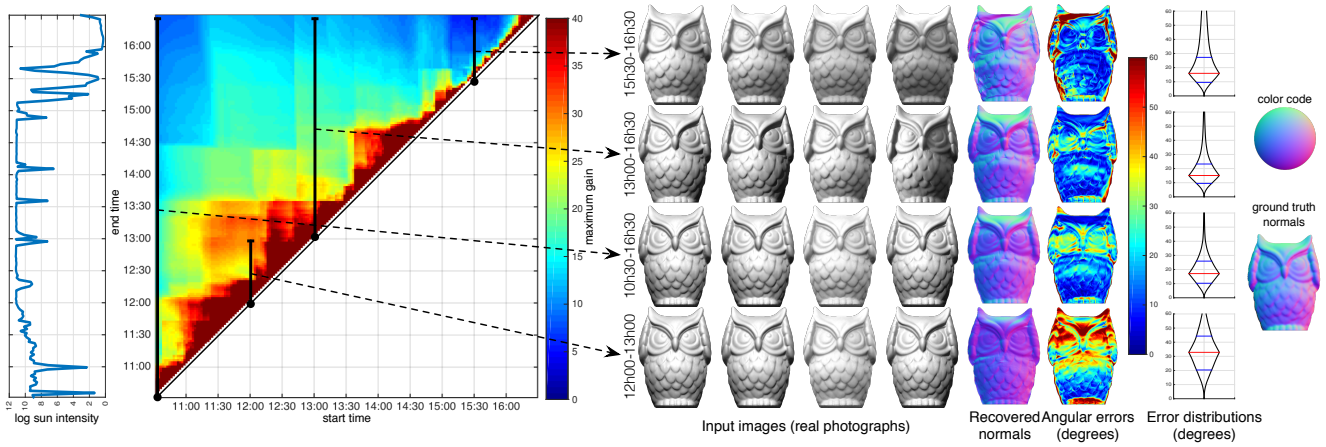


Figure 9. Validation on real data, captured on 11-OCT-14 (partly cloudy). Four distinct time intervals are analyzed and, for each one, the following information is displayed, from left to right: $(i)$ log sun intensity; $(ii)$ noise gain $\lambda_{\max}$ as a function of start time and duration of the interval, as in fig. 5; $(iii)$ example input images; $(iv)$ normals recovered by calibrated outdoor PS; $(v)$ normal estimation error at each pixel; and $(vi)$ the error distribution, in degrees. For reference, ground truth normals are given on the rightmost plots.

utes[1]. Ground truth surface normals were obtained by aligning a 3D model of the object (obtained with a 3D scanner) to the image using POSIT [8].

The validation results with real data are shown in fig. 9. As predicted by the noise gain values of fig. 9 (left), similar reconstruction performance is obtained from three different time intervals shown in the top three rows of fig. 9 (right). Once again, the performances of 1-hour (15:30–16:30) and 3.5-hour (13:00–16:30) outdoor PS are indeed quite close to that of "full-day" outdoor PS (10:30–16:30). However, not all one-hour intervals are equally good, as shown for the interval 12:00–13:00 at the bottom of fig. 9.

## 6. Conclusion

In this paper, we present what we believe is the first study of the time requirements for single-day outdoor PS. In particular, we seek to determine the relationship between expected performance in normal estimation and: $(i)$ the duration of data capture within a single, arbitrary day; and $(ii)$ specific atmospheric events that introduce beneficial lighting variations during that time interval. To achieve this goal, we use a large database of natural, outdoor illumination (sky probes) and take a detailed look at the conditions under which surface normals can be reconstructed reliably. Finally, we investigate whether these conditions are observed in less than a full day of data capture.

Our analysis reveals the following novel insights. First, we show how the mean light vectors (MLVs) are shifted from the solar plane when the sun is occluded by clouds. We demonstrate, through an extensive empirical analysis, that the atmospheric events causing that shift occur often in practice, and that they can be observed within a short time interval. In addition, we found that this shifting is often sufficient to constrain the PS problem significantly and reduce uncertainty in normal estimation. However, we also show that the shift is not the same for every normal; for some normals, shifting may not reduce uncertainty sufficiently. Finally, we validate our analysis by running calibrated outdoor PS on synthetic and real data.

One limitation of our work is that we consider only contiguous time intervals. It would be interesting to explore how non-consecutive images could be selected, from a given interval, with the goal of achieving additional improvements in performance. Presently, we are using the setup in fig. 8 to collect a database of real objects observed outdoors, and extending our analysis considering more elaborate shading and ground models.

We believe our findings open the way for interesting new research problems. Of note, one could leverage knowledge on MLV shifting to steer regularization in outdoor PS and even attempt to further reduce time requirements. It would also be interesting to include other cues, such as shape priors or stereo, to further constrain the problem. We plan to explore these issues in future work.

## Acknowledgments

The authors would like to thank Louis-Philippe Asselin and Marc-André Gardner for their help in developing the sky database website, and Julien Becirovski and Mathieu Garon for their help with data capture. This work was partially supported by the NSERC Discovery Grant RGPIN-2014-05314, FRQ-NT New Researcher Grant 2016NC189939, and a new faculty grant from the ECE department at Laval University. We gratefully acknowledge the support of NVIDIA Corporation with the donation of the Tesla K40 GPU used for this research.

[1]Data and source code are available on our project webpage [14].

## References


[1] A. Abrams, C. Hawley, and R. Pless. Heliometric stereo: Shape from sun position. In *European Conference on Computer Vision*, 2012.

[2] J. Ackermann, F. Langguth, S. Fuhrmann, and M. Goesele. Photometric stereo for outdoor webcams. In *IEEE Conference on Computer Vision and Pattern Recognition*, 2012.

[3] R. Aguiar and J. Page. *European Solar Radiation Atlas*. 3 edition, 1999.

[4] N. Alldrin, T. Zickler, and D. Kriegman. Photometric stereo with non-parametric and spatially-varying reflectance. In *IEEE Conference on Computer Vision and Pattern Recognition*, 2008.

[5] J. T. Barron and J. Malik. Shape, illumination, and reflectance from shading. *IEEE Transactions on Pattern Analysis and Machine Intelligence*, 37(8):1670–1687, Aug. 2015.

[6] R. Basri, D. Jacobs, and I. Kemelmacher. Photometric stereo with general, unknown lighting. *International Journal of Computer Vision*, 72(3):239–257, 2007.

[7] P. Debevec. Rendering synthetic objects into real scenes: bridging traditional and image-based graphics with global illumination and high dynamic range photography. In *Proceedings of ACM SIGGRAPH 1998*, pages 189–198, 1998.

[8] D. F. Dementhon and L. S. Davis. Model-based object pose in 25 lines of code. *International journal of computer vision*, 15(1-2):123–141, 1995.

[9] O. Drbohlav and M. Chantler. On optimal light configurations in photometric stereo. In *IEEE International Conference on Computer Vision*, 2005.

[10] W. W. Esty and J. D. Banfield. The box-percentile plot. *Journal of Statistical Software*, 8(i17):1–14, 2003.

[11] T. Hastie, R. Tibshirani, and J. Friedman. *The Elements of Statistical Learning: Data Mining, Inference, and Prediction*. Springer-Verlag, New York, NY, 2009.

[12] C. Hernández, G. Vogiatzis, and R. Cipolla. Overcoming shadows in 3-source photometric stereo. *IEEE Transactions on Pattern Analysis and Machine Intelligence*, 33(2):419–426, feb 2011.

[13] Y. Hold-Geoffroy, J. Zhang, P. F. U. Gotardo, and J.-F. Lalonde. What is a good day for outdoor photometric stereo? In *International Conference on Computational Photography*, 2015.

[14] Y. Hold-Geoffroy, J. Zhang, P. F. U. Gotardo, and J.-F. Lalonde. x-hour outdoor photometric stereo: Project webpage. http://vision.gel.ulaval.ca/~jflalonde/projects/xHourPS/, October 2015.

[15] C.-H. Hung, T.-P. Wu, Y. Matsushita, L. Xu, J. Jia, and C.-K. Tang. Photometric stereo in the wild. *2015 IEEE Winter Conference on Applications of Computer Vision*, 2015.

[16] K. Inose, S. Shimizu, R. Kawakami, Y. Mukaigawa, and K. Ikeuchi. Refining outdoor photometric stereo based on sky model. *Information and Media Technologies*, 8(4):1095–1099, dec 2013.

[17] M. K. Johnson and E. H. Adelson. Shape estimation in natural illumination. In *IEEE Conference on Computer Vision and Pattern Recognition*, 2011.

[18] J. Jung, J.-Y. Lee, and I. So Kweon. One-day outdoor photometric stereo via skylight estimation. In *IEEE Conference on Computer Vision and Pattern Recognition*, 2015.

[19] G. Oxholm and K. Nishino. Shape and reflectance from natural illumination. In *European Conference on Computer Vision*, 2012.

[20] F. Shen, K. Sunkavalli, N. Bonneel, S. Rusinkiewicz, H. Pfister, and X. Tong. Time-lapse photometric stereo and applications. *Computer Graphics Forum (Proc. Pacific Graphics)*, 33(7), Oct. 2014.

[21] B. Shi, K. Inose, Y. Matsushita, P. Tan, S.-K. Yeung, and K. Ikeuchi. Photometric stereo using internet images. *International Conference on 3D Vision*, 2014.

[22] J. Stumpfel, A. Jones, A. Wenger, C. Tchou, T. Hawkins, and P. Debevec. Direct HDR capture of the sun and sky. In *Proceedings of AFRIGRAPH*, 2004.

[23] R. Woodham. Photometric method for determining surface orientation from multiple images. *Opt. Eng.*, 19(1):139–144, feb 1980.

[24] L.-F. Yu, S.-K. Yeung, Y.-W. Tai, D. Terzopoulos, and T. F. Chan. Outdoor photometric stereo. In *IEEE International Conference on Computational Photography*, 2013.